



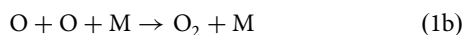
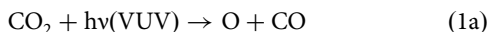
## Direct production of molecular oxygen from carbon dioxide and helium ion collisions

Yaya Zhi<sup>1</sup>, Qiang Guo<sup>1</sup>, Jingchen Xie<sup>1</sup>, Jie Hu<sup>2</sup>  <sup>✉</sup> & Shan Xi Tian<sup>1,2,3</sup>  <sup>✉</sup>

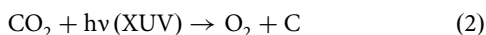
The prebiotic mechanism to produce molecular oxygen (O<sub>2</sub>) in carbon dioxide (CO<sub>2</sub>)-rich planetary atmospheres is of great importance in understanding astrochemical reactions and is potentially relevant to the origin of life on Earth. Here, we demonstrate that, aside from the direct productions of O<sub>2</sub> by photodissociation and dissociative electron attachment, the low-energy ion-molecule reaction between cationic helium in solar winds and molecular CO<sub>2</sub> is a noticeable mechanism. Branching ratios of the reaction channels are determined, and their absolute cross-sections are estimated accordingly. The present findings represent a further, indispensable step towards fully understanding the origins of atmospheric O<sub>2</sub>.

<sup>1</sup>Department of Chemical Physics, Collaborative Innovation Center of Chemistry for Energy Materials (iChEM), University of Science and Technology of China, 230026 Hefei, China. <sup>2</sup>Hefei National Research Center for Physical Sciences at the Microscale, University of Science and Technology of China, 230026 Hefei, China. <sup>3</sup>Hefei National Laboratory, University of Science and Technology of China, 230088 Hefei, China. ✉email: [jjehu@ustc.edu.cn](mailto:jjehu@ustc.edu.cn); [sxtian@ustc.edu.cn](mailto:sxtian@ustc.edu.cn)

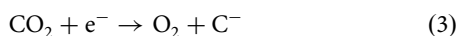
Before the dramatic rise of atmospheric oxygen during the *Great Oxidation Event* about 2.4 billion years ago on Earth<sup>1,2</sup>, few oxygen molecules (O<sub>2</sub>) already existed in the primitive atmosphere which was nearly full of carbon dioxide (CO<sub>2</sub>). Those O<sub>2</sub> molecules were exclusively produced via abiotic processes. A widely accepted mechanism about the O<sub>2</sub> origin in CO<sub>2</sub>-rich planetary atmosphere is the cascade process induced with vacuum ultraviolet (VUV) photon



where the product O<sub>2</sub> can be stabilized efficiently by releasing a third body M<sup>3-5</sup>. A recent experimental study indicated that O<sub>2</sub> was directly produced in near extreme ultraviolet (XUV) photodissociation<sup>6</sup>

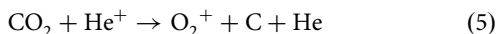
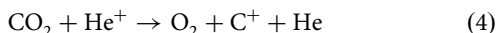


More recently, we reported another finding that dissociative electron attachment (DEA) also directly led to the O<sub>2</sub> formation<sup>7</sup>



Since a large quantity of low-energy free electrons were detected in the atmospheres of Venus and Mars, as well as the current Earth<sup>8-11</sup>, Eq. (3) and relevant DEA processes that were unheeded over a long period should be incorporated into the atmospheric reaction networks.

Besides VUV/XUV photons and free electrons, He<sup>2+</sup> (alpha particle) and He<sup>+</sup> are the heavy (relative to H<sup>+</sup>) ions in the solar wind<sup>12-15</sup>. Although the He<sup>+</sup>/He<sup>2+</sup> collisional reactions were confirmed to contribute to the production of O<sup>+</sup>, O<sub>2</sub><sup>+</sup>, and CO<sub>2</sub><sup>+</sup> in the Martian ionosphere<sup>16,17</sup>, there is still no indisputable evidence about the O<sub>2</sub> formation<sup>18-20</sup>. Here we demonstrate that O<sub>2</sub> and O<sub>2</sub><sup>+</sup> are certainly produced in the following collisional reactions:



by the measurements of time-of-flight (TOF) mass spectra and ion velocity maps using a crossed-beam apparatus<sup>21-23</sup>.

Previously, the experimental drawbacks such as multiple collisions and ionic yield collection or transportation gave rise to a divergence in whether O<sub>2</sub> or O<sub>2</sub><sup>+</sup> could be produced in the thermal-energy reactions of He<sup>+</sup> + CO<sub>2</sub> (refs. 18-20), while those technical troubles are settled in the present measurements. On the other hand, the translational energy of He<sup>+</sup> in the Martian atmosphere spreads over a wide range and depends on its sources, for instance, the velocity of He<sup>+</sup> is comparable to that of He<sup>2+</sup> in the solar wind if He<sup>+</sup> is produced by the charge exchange reaction between He<sup>2+</sup> and neutral hydrogen<sup>13</sup>. Besides the thermal-energy collisions, He<sup>+</sup> + CO<sub>2</sub> reactions at the collision energy of electron volts are particularly interesting, since the products in different electronic states, as shown in Fig. 1, play versatile roles in the subsequent processes.

CO<sub>2</sub><sup>+</sup> formed in the resonant charge exchange between CO<sub>2</sub> and He<sup>+</sup> can be populated in the ro-vibrationally excited states of electronic state  $\tilde{\text{C}}^2\Sigma_g^+$  or the  $^2\Pi_u$ -satellite states, but its spontaneous dissociation is highly preferred due to an electron depletion from the bonding orbital 4σ<sub>g</sub> or 1π<sub>u</sub> of CO<sub>2</sub> (refs. 24,25). The channels producing CO<sup>+</sup> + O and O<sup>+</sup> + CO were found to be dominant in the thermal collisions of He<sup>+</sup> + CO<sub>2</sub> (refs. 18-20,26), and as one of their subsequent processes, the photoemission  $\tilde{\text{A}}^2\Pi \rightarrow \tilde{\text{X}}^2\Sigma^+$  of the CO<sup>+</sup> yield may contribute to the comet tail glow<sup>26</sup>. Such scenarios can be further found in Fig. 1. For instance, the phosphorescence from the O<sub>2</sub> in singlet states (*a*<sup>1</sup>Δ<sub>g</sub>, *b*<sup>1</sup>Σ<sub>g</sub><sup>+</sup>)

was observed in the aurora<sup>27</sup>. The reactions noted in Fig. 1, once authenticated experimentally, should be of fundamental importance toward understanding the oxygen-related processes in planetary atmospheres.

The present experiments were conducted with our home-made crossed-beam apparatus which was recently updated by introducing the three-dimensional velocity map imaging technique of ionic products<sup>22,23</sup>. The TOF mass spectra and velocity distributions of all ionic yields can be obtained simultaneously. The collection efficiency of ionic yields is close to 100%, and each peak in the TOF mass spectrum corresponds to the whole Newton spheres of a certain type of ionic yield. The multiple collisions in the ion flowing or the ion drift of cyclotron resonance<sup>18-20</sup> are absent or reduced significantly in the crossed-beam arrangement where the pulsed reactant ion beam is perpendicular to a supersonic target beam.

Due to the energy redistribution in a collision, the endothermic channels (their energetic thresholds can be found in Table S1 of Supplementary Note 1) in Fig. 1 are possibly accessed. For example, around 3.5 eV of the collision energy, the reactions leading to O<sub>2</sub>( $\tilde{\text{X}}^3\Sigma_g^-$ ) + C<sup>+</sup>(<sup>4</sup>P<sub>1/2</sub>) and 2O(<sup>3</sup>P<sub>2</sub>) + C<sup>+</sup>(<sup>2</sup>P<sub>1/2</sub>) are allowed in energetics if the collisional or translational energy is completely transformed into the internal energies of the target. However, in the TOF mass spectrometry measurement, the same product, C<sup>+</sup> as mentioned above, cannot be distinguished from which channel the ion originates. Different ion production channels could be further identified by the ion velocity imaging measurements. In this work, the combinational measurements were accomplished at three collision energies in the reaction center-of-mass (c.m.) coordinate (*E*<sub>c.m.</sub> = 1.94, 2.49, and 4.75 eV).

## Results and discussion

The TOF mass spectrum at *E*<sub>c.m.</sub> = 4.75 eV, as a typical example, is shown in Fig. 2a, in which the C<sup>+</sup> and O<sub>2</sub><sup>+</sup> ions are observed clearly but their relative intensities are much lower than those of other ionic yields. Such low signals of C<sup>+</sup> and O<sub>2</sub><sup>+</sup> certainly brought difficulties in the previous measurements<sup>18-20,26</sup>. Here, we further obtained the branching ratios of the reactions and plotted their collision energy dependences in Fig. 2b. A comparison between the present branching ratios and the previous ones<sup>18-20</sup> is presented in Table S2 of Supplementary Note 2.

In the reactions at the higher collision energies (10–10<sup>3</sup> eV), the production ratio γ (C<sup>+</sup>/CO<sup>+</sup>) was found to gradually increase with the enhancement of He<sup>+</sup> kinetic energy<sup>24</sup>. Here one can find that the branching ratios of the reactions denoted with Eqs. (4) and (5) decrease with the *E*<sub>c.m.</sub> enhancement. Such different collision-energy dependences should be attributed to reaction dynamics, e.g., diversities of collisional trajectories and dissociation pathways. Usually, the time scale of a charge exchange at the higher collision energy could be shorter than that of molecular vibrational motions. O<sub>2</sub> can only be formed via the slow atomic roaming<sup>6</sup> or the bending motion with a large amplitude of CO<sub>2</sub> (ref. 7). Thereby, similar scenarios should exist for the O<sub>2</sub> or O<sub>2</sub><sup>+</sup> product of the He<sup>+</sup> + CO<sub>2</sub> reactions at the lower collision energy.

The velocity maps of C<sup>+</sup> and O<sub>2</sub><sup>+</sup> products in Fig. 3 correspond to the ionic three-dimensional Newton spheres projected on the detector or reaction plane, rather than the central slices of the spheres. Nevertheless, we still can find the collision-energy dependences of the velocity distributions. Figure 3a indicates that the C<sup>+</sup> yields are primarily located around the target CO<sub>2</sub> at the lower collision energies, but most of them are distributed in the forward direction (namely the CO<sub>2</sub> flying direction) at *E*<sub>c.m.</sub> = 4.75 eV. In contrast to the C<sup>+</sup> velocity maps, as shown in Fig. 3b, most of the O<sub>2</sub><sup>+</sup> ions are always distributed around CO<sub>2</sub> and become crowded at *E*<sub>c.m.</sub> = 4.75 eV. The forward scattering

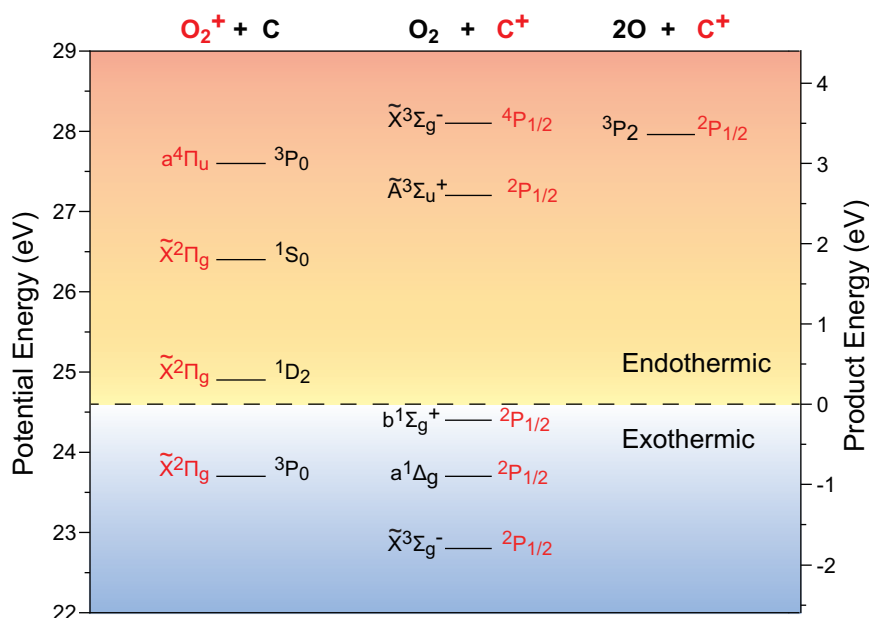


**Fig. 1** Asymptotic energies of three charge-exchange reactions between  $\text{He}^+$  and  $\text{CO}_2$ . The product energy is scaled, concerning the zero value for the resonant charge exchange of the motionless reagents  $\text{He}^+(^2S) + \text{CO}_2(\tilde{X}^1\Sigma_g^-)$ . Besides the exothermic pathways, the endothermic processes could proceed if the collision energy is available transformed.

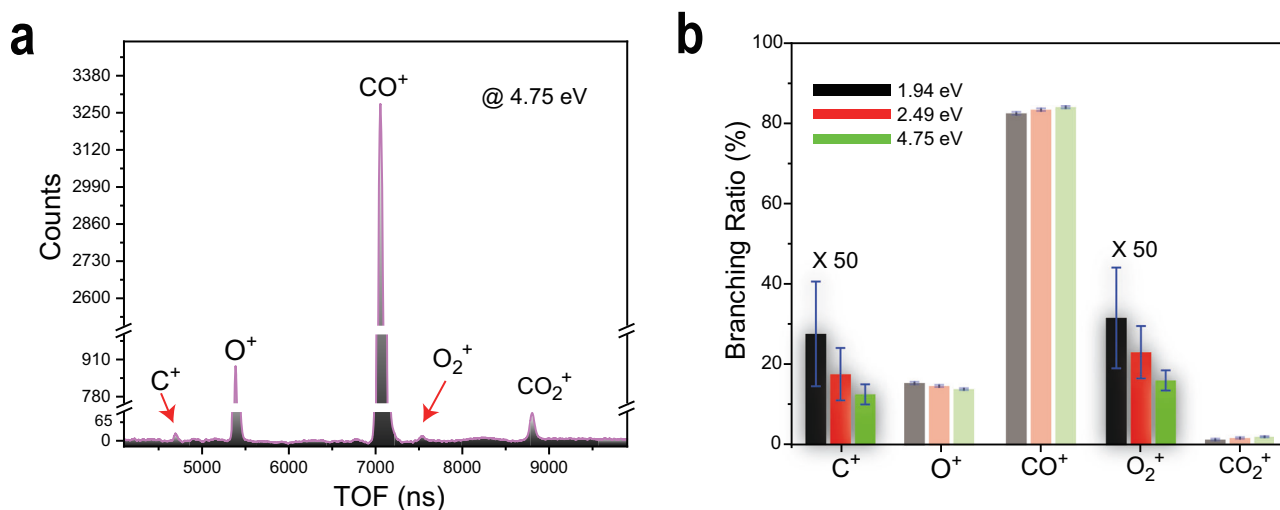


**Fig. 2** Ionic yields of the collisional reaction between  $\text{He}^+$  and  $\text{CO}_2$  at 4.75 eV **(a)** and branching ratios **(b)**. **a** Time-of-flight (TOF) mass spectrum is plotted with the real ion counts. **b** Branching ratios (with the statistic uncertainties of the measurements) of  $\text{O}_2^+$  and  $\text{C}^+$  yields are amplified to be more visible.

preference and the product distributions around the reactant  $\text{CO}_2$  indicate that the reactions would like to proceed in the large-parameter collisions, namely, the collisional or translational energy is hardly transferred to the target in such a contactless reaction. Therefore, the higher-threshold channel leading to the fragments  $2\text{O}(^3P_2) + \text{C}^+(^2P_{1/2})$  is unfavorable at  $E_{\text{c.m.}} = 4.75$  eV, due to the inefficient translational-to-internal energy transformation. The isotropic angular distributions (red circles in Fig. 3) represent the  $\text{C}^+$  yield of the  $\text{CO}_2^+$  dissociation where  $\text{CO}_2^+$  is assumed to be rebounded toward the c.m. position and receives 4.75 eV in a head-on collision. What we observed here obviously deviates from this hypothetical model.

The  $\text{O}_2$  coproduct is likely in  $b^1\Sigma_g^+$  at the lower collision energies, primarily due to near energy-resonance of the channel to  $\text{O}_2(b^1\Sigma_g^+) + \text{C}^+(^2P_{1/2})$  (see Fig. 1) and partially according to

the velocity  $u(\text{C}^+)$  distributions in Fig. S1a. The  $\text{O}_2$  coproduct could be in  $\tilde{X}^3\Sigma_g^-$  or  $\tilde{A}^3\Sigma_u^+$  state at the higher collision energy 4.75 eV. The  $u(\text{O}_2^+)$  profiles in Fig. S1b, by contrast, exhibit a preference for the ground-state product  $\text{O}_2^+(\tilde{X}^2\Pi_g)$ .  $\text{O}_2$  or  $\text{O}_2^+$  in other states could be produced as the minor yields. More importantly, the absolute cross sections or production efficiencies of  $\text{O}_2$  and  $\text{O}_2^+$  are the fundamental data of atmospheric reaction networks, but very few are available so far<sup>18–20,24,26,28,29</sup>. Extrapolating the total cross-sections of the  $\text{He}^+ + \text{CO}_2$  reaction (all channels) from the higher collision energies<sup>28,29</sup> to the low-energy range and according to the branching ratios obtained in this work, we further derive the absolute cross-sections of about  $10^{-22} \text{m}^2$  of the reactions denoted with Eqs. (4) and (5) in a collision energy range of 1–5 eV (more details can be found in Supplementary Note 3).

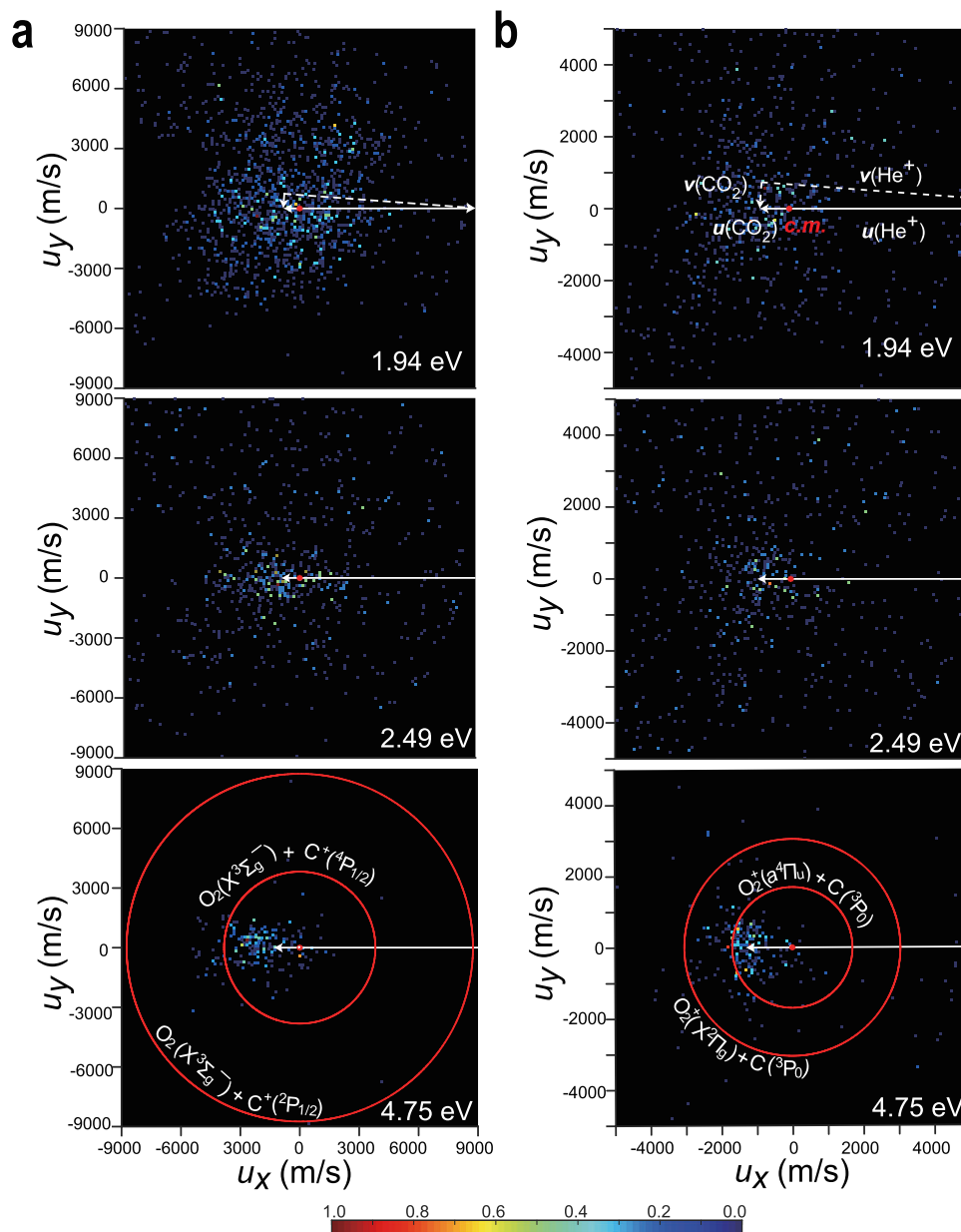


**Fig. 3 Velocity map images of  $C^+$  (a) and  $O_2^+$  (b).** Each velocity image is the projection of three-dimensional Newton spheres of  $C^+$  or  $O_2^+$  to the ion detector. Red circles represent the isotropic distributions for  $O_2(\tilde{X}^3\Sigma_g^-) + C^+(^4P_{1/2})$  (inner circle) and  $O_2(\tilde{X}^3\Sigma_g^-) + C^+(^2P_{1/2})$  (outer circle) or  $O_2^+(\tilde{X}^2\Pi_u) + C(^3P_0)$  (outer circle) and  $O_2^+(\tilde{a}^4\Pi_u) + C(^3P_0)$  (inner circle) yields that are assumed to be produced in photodissociation of  $CO_2^+$  at the center-of-mass (c.m.) of the collision. White lines with arrows show the coordinate transformation from the laboratory (the reactants' velocities are represented with  $v$ , broken lines) and the collisional c.m. coordinate (the reactants' velocities are represented with  $u$ , solid lines). The ionic signals in the left and right sides respective to c.m. are defined as the forward and backward scatterings.

These cross-sections are a few hundred times larger than that of the direct production of  $O_2$  via DEA<sup>7</sup>.

As discussed previously, oxygen-atom roaming and molecular bending are two feasible pathways to produce  $O_2$  from  $CO_2$ , where the former usually results in the nearly isotropic angular distributions of the products while a distinct anisotropy can be observed for the latter<sup>6,7</sup>. As proposed above, in the large-parameter collisional reaction, the He atom formed by the prompt charge exchange should be a spectator in the subsequent dissociation. To further reveal this unimolecular-like process, we make a coordinate transformation from the reaction c.m. one (used in Fig. 3) to the  $CO_2$  reaction coordinate (more details can be found in Supplementary Note 4). As illustrated in Fig. S2, the  $CO_2$  reaction coordinate is also defined with respect to the

collision axis, but its scattering angle is different from that in the reaction c.m. coordinate. Figure 4 shows the angular and velocity distributions of  $C^+$  and  $O_2^+$  in the  $CO_2$  reaction coordinate.

Figure 4a exhibits the nearly isotropic distributions of  $C^+$  at the lower  $E_{c.m.}$  values and a clearly forward preference at 4.75 eV, where  $O_2$  and  $C^+$  yields are assumed to be in specific states. As indicated in Fig. S3, this collision-energy dependence scarcely relies on the products' states. A cartoon in the bottom panel of Fig. S3b illustrates a possible molecular orientation, namely, the dissociation undergoes the bended conformation which is almost perpendicular to the collision axis. It is reasonable that such a stereodynamics feature becomes indistinct in the slower collisional reaction. All  $O_2^+$  angular distributions in Fig. 4c are almost isotropic, which could be attributed to the roaming dynamics,

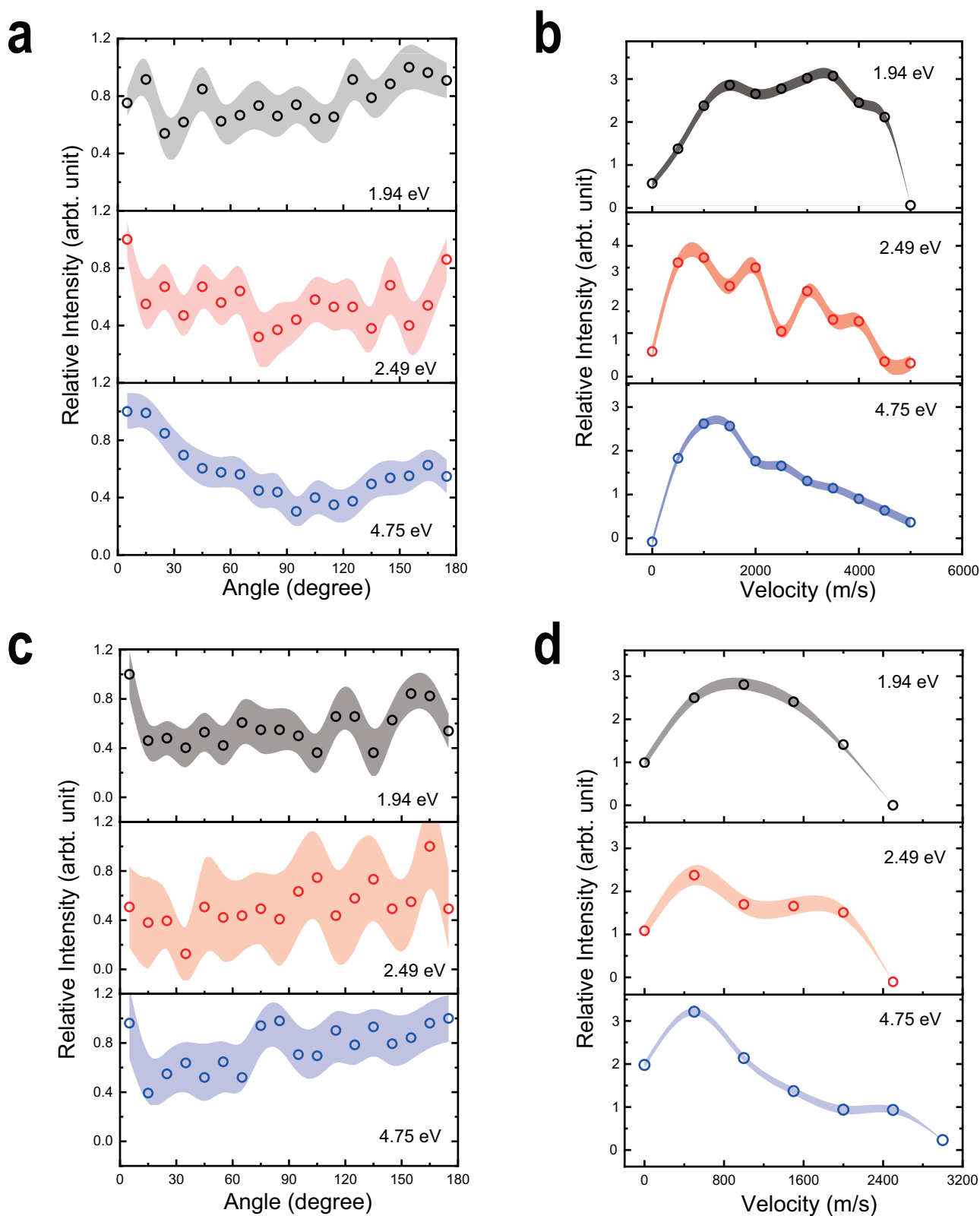


**Fig. 4** Angular and speed distributions of  $C^+$  (a, b) and  $O_2^+$  (c, d) yields. These distributions after the independent intensity normalizations are plotted in the  $CO_2$  reaction coordinate by the transformation from those in the collisional c.m. coordinate and assuming the reactions lead to  $O_2(b^1\Sigma_g^+) + C^+(^2P_{1/2})$  (a, b) or  $O_2(^{\tilde{X}}^2\Pi_g) + C(^3P_0)$  (c, d). The shades in different colors represent the statistical uncertainties and the ion intensities are normalized independently. Each point in the angular distribution (a, c) corresponds to all ion signals within a range of  $\pm 5^\circ$ .

namely, the roaming  $O^+$  abstracts the oxygen atom from the  $CO$  moiety. The velocities of  $C^+$  and  $O_2^+$  in Fig. 4b and d indicate the lower values at the higher collision energy, due to an enhancement of the products in the higher states.

To further understand the dissociation dynamics of  $CO_2^+$ , we plot the potential energy surfaces of  $\tilde{C}^2\Sigma_g^+$  state in Fig. S4 of Supplementary Note 5. Different shapes or patterns of above potential energy surfaces imply that the  $O_2^+$  or  $O_2$  formation hardly undergoes a combinational motion of molecular bending and symmetric bond stretching, but possibly benefits from an asymmetric stretching. The asymmetric stretching should be also responsible for the predominance of the  $CO^+$  and  $O^+$  products observed in this work and the previous studies<sup>18–20,24,26,28,29</sup>. However, it would be a tough task to simulate the dynamic trajectories leading to  $O_2$  or  $O_2^+$  because of their much lower yields. Furthermore, the nonadiabatic process, for instance, coupling between  $\tilde{C}^2\Sigma_g^+$  state and  $^2\Pi_u$ -satellite states of  $CO_2^+$ <sup>25</sup>, may be involved in the reactions.

## Conclusions

Based on the previous and present findings, we make a conclusive remark on the origins of atmospheric  $O_2$ . Since the production efficiency of the photodissociation of  $CO_2$  was not high enough to reproduce the measured data<sup>30</sup>, the other production sources of those  $O_2$  molecules must be considered. The  $He^+ + CO_2$  reaction, particularly in the low collision energy range, is an important mechanism but was ignored before this study. Up to date, we have known different mechanisms for the origin of atmospheric  $O_2$ . The  $O$  atoms produced in the ion-molecule reaction, DEA, and photodissociation can also participate in the formation of  $O_2$ . Some contributions could be from the  $O^+$  and  $O_2^+$  ions by the electron capture, however, these ions are likely responsible for the oxygen escaping<sup>16,17</sup>. All-inclusive networks of the atmospheric and interstellar oxygen-related reactions are expected to be established by more and more laboratory studies and astronomical observations.

## Methods

**Experiments.** Our three-dimensional velocity map imaging apparatus has been described elsewhere<sup>22</sup>, in which the product ion detector consists of a set of multichannel plates and a Delay-Line-Detector (DLD  $\phi = 80$  mm, commercially available from Roentdek). The ion source that previously produced  $Ar^+$  ions<sup>21</sup> was updated recently to produce lighter ions (such as  $He^+$ ). In the present experiment, the energy spreads ( $\Delta E/E \sim 7\%$ ) of the  $He^+$  bunches are comparable to that of the  $Ar^+$  bunches. The  $x$ - $y$  positions (the plane of the detector) and the time of flight (along  $z$  direction) of each ionic signal are recorded simultaneously with the DLD, and then a Newton sphere of a certain type of ionic yield is rebuilt with these data<sup>22,23</sup>. In Fig. 3, the two-dimensional images are plotted with the raw data of whole Newton spheres of the ionic products projected on the detector, where one pixel corresponds to ca. 200 m/s of  $C^+$  or  $O_2^+$ . On the other hand, the TOF mass spectrum can be directly obtained from the measurement of whole Newton spheres, thus the ion collection efficiency is nearly 100%. High-purity (99.99%) samples ( $He$  and  $CO_2$ ) are available commercially and used without further purification. The  $He^+$  reactant ions are produced in the electron impacts at 30 eV. The kinetic energies and the energy spreads of the reactants  $He^+$  and  $CO_2$  (its  $\Delta E/E \sim 6\%$ ) were calibrated or determined prior to the experiments. During the experiments, the reaction chamber is evacuated under a steady vacuum condition of  $2.0 \times 10^{-7}$  mbar and the reactions happen in the field-free region. The working frequency is 10 kHz, and we

need dozens of hours to record the velocity images at a given collision energy.

**Calculations.** Equilibrium geometry and vibrational frequencies of the ground-state  $CO_2$  were calculated at the density functional theory level wb97xd/def2TZVP. This molecular geometry was used as the initial point in scanning the potential energy surfaces along the vibrational motions, i.e., symmetric stretching Q1, bending Q2, and asymmetric stretching Q3. Table S4 shows the corresponding values of real bond length and bond angle for each Q1–Q3. The equation of motion method based on the coupled cluster method limited to singles and doubles excitations and the basis set cc-pVTZ<sup>31–34</sup> (encoded in Gaussian16 suit of programs<sup>35</sup>) were used here to obtain the two-dimensional potential energy surfaces of  $CO_2^+(C^2\Sigma_g^+)$ .

## Data availability

All data underlying the figures are deposited in the main text or as supplementary information. The calculated data about the potential energy surfaces of  $CO_2^+(C^2\Sigma_g^+)$  are available upon the requests to the corresponding authors.

Received: 17 July 2023; Accepted: 22 November 2023;

Published online: 06 December 2023

## References

1. Canfield, D. E. The early history of atmospheric oxygen. *Annu. Rev. Earth Planet. Sci.* **33**, 1–36 (2005).
2. Bekker, A. et al. Dating the rise of atmospheric oxygen. *Nature* **427**, 117–120 (2004).
3. Kasting, J. F., Liu, S. & Donahue, T. Oxygen levels in the prebiological atmosphere. *J. Geophys. Res.* **84**, 3097–3107 (1979).
4. Kasting, J. F. & Walker, J. C. Limits on oxygen concentration in the prebiological atmosphere and the rate of abiotic fixation of nitrogen. *J. Geophys. Res.* **86**, 1147–1158 (1981).
5. Kasting, J. F., Pollack, J. B. & Crisp, D. Effects of high  $CO_2$  levels on surface temperature and atmospheric oxidation state of the early Earth. *J. Atmos. Chem.* **1**, 403–428 (1984).
6. Lu, Z., Chang, Y.-C., Yin, Q.-Z., Ng, C. Y. & Jackson, W. M. Evidence for direct molecular oxygen production in  $CO_2$  photodissociation. *Science* **346**, 61–64 (2014).
7. Wang, X.-D., Gao, X.-F., Xuan, C.-J. & Tian, S. X. Dissociative electron attachment to  $CO_2$  produces molecular oxygen. *Nat. Chem.* **8**, 258–263 (2016).
8. Pätzold, M. et al. The structure of Venus' middle atmosphere and ionosphere. *Nature* **450**, 657–660 (2007).
9. Frahm, R. A. et al. Carbon dioxide photoelectron energy peaks at Mars. *Icarus* **182**, 371–382 (2006).
10. Lee, J. S., Doering, J. P., Potemral, T. A. & Brace, H. Measurements of the ambient photoelectron spectrum from atmosphere explorer: I. AE-E measurements below 300 km during solar minimum conditions. *Planet. Space Sci.* **28**, 947–971 (1980).
11. Mantas, G. P. & Hanson, W. B. Photoelectron fluxes in the Martian ionosphere. *J. Geophys. Res.* **84**, 369–385 (1979).
12. Möbius, E. et al. Direct observation of  $He^+$  pick-up ions of interstellar origin in the solar wind. *Nature* **318**, 426–429 (1985).
13. Swaczyna, P., McComas, D. J. & Zirnstein, E. J.  $He^+$  ions comoving with the solar wind in the outer heliosphere. *Astrophys. J.* **875**, 36 (2019).
14. Barabash, S. & Norberg, O. Indirect detection of the Martian helium corona. *Geophys. Res. Lett.* **21**, 1547–1550 (1994).
15. Halekas, J. S. & MaFadden, J. P. Using solar wind helium to probe the structure and seasonal variability of the Martian hydrogen corona. *J. Geophys. Res.: Planets* **126**, e2021JE007049 (2021).
16. Kallio, E. et al. Energisation of  $O^+$  and  $O_2^+$  ions at Mars: an analysis of a 3-D quasi-neutral hybrid model simulation. *Space Sci. Rev.* **126**, 39–62 (2006).
17. Maes, L., Fraenz, M., McFadden, J. P. & Benna, M. Escape of  $CO_2^+$  and other heavy minor ions from the ionosphere of Mars. *J. Geophys. Res.: Space Phys.* **126**, e2020JA028608 (2021).
18. Fehsenfeld, F. C., Schmeltekopf, A. L., Goldan, P. D., Schiff, H. I. & Ferguson, E. E. Thermal energy ion-neutral reaction rates. I. Some reactions with helium ions. *J. Chem. Phys.* **44**, 4087–4098 (1966).

19. Adams, N. G. & Smith, D. Product-ion distributions for some ion-molecule reaction. *J. Phys. B: Mol. Phys.* **9**, 1439–1450 (1976).
20. Anicich, V. G., Laudenslager, J. B., Huntress, W. T. Jr. & Futrell, J. H. Product distributions for some thermal energy charge transfer reactions of rare gas ions. *J. Chem. Phys.* **67**, 4340–4350 (1977).
21. Hu, J., Wu, C.-X. & Tian, S. X. A well-confined pulsed low-energy ion beam: test experiments of Ar<sup>+</sup>. *Rev. Sci. Instrum.* **89**, 066104 (2018).
22. Hu, J. et al. Stereodynamics observed in the reactive collisions of low-energy Ar<sup>+</sup> with randomly oriented O<sub>2</sub>. *J. Phys. Chem. Lett.* **12**, 1346–1351 (2021).
23. Hu, J., Zhi, Y.-Y., Xie, J.-C., Wu, C.-X. & Tian, S. X. Collision-energy dependent stereodynamics of the dissociative charge exchange reaction between Ar<sup>+</sup> and CO. *J. Phys. Chem. Lett.* **12**, 7127–7133 (2021).
24. McMillan, M. R. & Coplan, M. A. Kinematics of He<sup>+</sup>–CO<sub>2</sub> dissociative charge exchange. *J. Chem. Phys.* **71**, 3063–3071 (1979).
25. Roy, P., Nenner, I., Millie, P., Morin, P. & Roy, D. Experimental and theoretical study of configuration interaction states of CO<sub>2</sub><sup>+</sup>. *J. Chem. Phys.* **84**, 2050–2061 (1980).
26. Tsuji, M., Endoh, M., Susuki, T., Mizukami, K. & Nishimura, Y. Optical spectroscopic study of thermal-energy charge transfer between He<sup>+</sup> and CO<sub>2</sub>. *J. Chem. Phys.* **81**, 3559–3563 (1984).
27. Burrage, M. D., Arvin, N., Skinner, W. R. & Hay, P. B. Observations of the O<sub>2</sub> atmospheric band nightglow by the high-resolution Doppler imager. *J. Geophys. Res.* **99**, 15017–15023 (1994).
28. Parker, J. E. & Johnson, C. A. F. A two-state treatment of the electron transfer reactions from carbon dioxide to helium ions. *Int. J. Mass Spectrom. Ion-Proc.* **94**, 87–99 (1989).
29. Werbowy, S. & Pranszke, B. Charge-exchange processes in collisions of H<sup>+</sup>, H<sub>2</sub><sup>+</sup>, H<sub>3</sub><sup>+</sup>, He<sup>+</sup>, and He<sub>2</sub><sup>+</sup> ions with CO and CO<sub>2</sub> molecules at energies below 1000 eV. *Phys. Rev. A.* **93**, 022713 (2016).
30. Lo, D. Y., Yelle, R. V. & Lillis, R. J. Carbon photochemistry at Mars: updates with recent data. *Icarus* **352**, 114001 (2020).
31. Kendall, R. A., Dunning, T. H. Jr. & Harrison, R. J. Electron affinities of the first-row atoms revisited. Systematic basis sets and wave functions. *J. Chem. Phys.* **96**, 6796–6806 (1992).
32. Dunning, T. H. Jr. Gaussian basis sets for use in correlated molecular calculations. I. The atoms boron through neon and hydrogen. *J. Chem. Phys.* **90**, 1007–1023 (1989).
33. Woon, D. E. & Dunning, T. H. Jr. Gaussian-basis sets for use in correlated molecular calculations. III. The atoms aluminum through argon. *J. Chem. Phys.* **98**, 1358–1371 (1993).
34. Peterson, K. A., Woon, D. E. & Dunning, T. H. Jr. Benchmark calculations with correlated molecular wave functions. IV. The classical barrier height of the H + H<sub>2</sub> → H<sub>2</sub> + H reaction. *J. Chem. Phys.* **100**, 7410–7415 (1994).
35. Frisch, M. J. et al. *Gaussian 16, Revision C.01* (Gaussian, Inc., Wallingford, CT, 2019).

## Acknowledgements

We gratefully acknowledge the financial support from the Strategic Priority Research Program of the Chinese Academy of Sciences (XDB0450202) and the National Natural Science Foundation of China (22233004, 22003062). The numerical calculations are done in the Supercomputing Center of the University of Science and Technology of China.

## Author contributions

S.X.T. conceived this study. S.X.T. and J.H. supervised this study. Y.Z., Q.G., and J.H. carried out the experiments. Y.Z. and J.X. performed the quantum chemistry calculations. Y.Z., Q.G., and J.H. did the data analyses. All authors contributed to the discussion and the manuscript preparation.

## Competing interests

The authors declare no competing interests.

## Additional information

**Supplementary information** The online version contains supplementary material available at <https://doi.org/10.1038/s42004-023-01074-2>.

**Correspondence** and requests for materials should be addressed to Jie Hu or Shan Xi Tian.

**Peer review information** *Communications Chemistry* thanks the anonymous reviewers for their contribution to the peer review of this work.

**Reprints and permission information** is available at <http://www.nature.com/reprints>

**Publisher's note** Springer Nature remains neutral with regard to jurisdictional claims in published maps and institutional affiliations.



**Open Access** This article is licensed under a Creative Commons

Attribution 4.0 International License, which permits use, sharing, adaptation, distribution and reproduction in any medium or format, as long as you give appropriate credit to the original author(s) and the source, provide a link to the Creative Commons license, and indicate if changes were made. The images or other third party material in this article are included in the article's Creative Commons license, unless indicated otherwise in a credit line to the material. If material is not included in the article's Creative Commons license and your intended use is not permitted by statutory regulation or exceeds the permitted use, you will need to obtain permission directly from the copyright holder. To view a copy of this license, visit <http://creativecommons.org/licenses/by/4.0/>.

© The Author(s) 2023